Advanced Materials Science and Technology Vol 4 Issue 2 2022
DOI: 10.37155/2717–526X–0402–6

ORIGINAL RESEARCH ARTICLE

Open Access

Omniscient Pte.Ltd.

The Activated Carbon with Pyrolle-N from Cotton Stalk for the Electrochemical Performance

Tie-Zhen Ren[1,2,*], Meng-Jie Cui[1], Yan-Mei Zhao[2], Wen-Long Mo[1], Zheng Wang[3]

[1]State Key Laboratory of Chemistry and Utilization of Carbon Based Energy Resources and Key Laboratory of Coal Clean Conversion & Chemical Engineering Process (Xinjiang Uyghur Autonomous Region), College of Chemical Engineering, Xinjiang University, Urumqi 830046, China.
[2]Hebei Provincial Key Laboratory of Green Chemical Technology & High Efficient Energy Saving, School of Chemical Engineering and Technology, Hebei University of Technology, Tianjin 300130, China.
[3]State Key Laboratory of High-efficiency Utilization of Coal and Green Chemical Engineering, Ningxia University, Yinchuan 750021, China.

***Correspondence to:** Tie-Zhen Ren, State Key Laboratory of Chemistry and Utilization of Carbon Based Energy Resources and Key Laboratory of Coal Clean Conversion & Chemical Engineering Process (Xinjiang Uyghur Autonomous Region), College of Chemical Engineering, Xinjiang University, Urumqi 830046, China. Email: rtz@xju.edu.cn

Received: October 18, 2022; **Accepted:** December 29, 2022; **Published Online:** December 31, 2022

Citation: Ren TZ, Cui MJ, Zhao YM, Mo WL and Wang Z. The Activated Carbon with Pyrolle-N from Cotton Stalk for the Electrochemical Performance. *Advanced Materials Science and Technology*, 2022;4(2):0410212. https://doi.org/10.37155/2717-526X-0402-6

Abstract: Porous carbon materials have been applied in many fields for their advanced physical features. Using biomass waste material as the activated carbon (AC) source is of importance to keep the sustainable environment. The CO_2 activation and KOH activation were adopted to create AC with the flexible porous structure and the former caused low surface area but with high nitrogen content of AC. The reversed results were formed with the KOH activation. The differences on specific surface area and nitrogen groups distribution were investigated by nitrogen sorption isotherm and X-ray photoluminescence spectroscopy. Their porous structure and framework were characterized with transmission electron microscope and Raman spectra. Electrochemical performance was evaluated by supercapacitance and oxygen evolution reaction (OER). Comparing to the CO_2 activation, KOH activation improved surface area of AC and more functional groups on the carbon surface, which led to the enhancement of the electroactivity.

Keywords: Activated carbon; Porous structure; Surface feature; Supercapacitance; OER

1. Introduction

Facing the double pressure of environment and energy, advanced research on catalysts for energy storage and conversion, such as fuel cells[1], metal air batteries[2-4], lithium sulfur batteries[5], supercapacitor[6-8], and water splitting[9] have been developed. Carbon materials are free from the constraints of precious metal materials (Pt, Ru, Au) and possess the long life and stable activity[10-12]. Nowadays, one-, two- or three-dimensional carbon materials from biomass have been used as functional catalysts[13-16]. Among them the hierarchically porous activated carbon (AC) has been attracted much attention with high surface area and pore volume[2-4]. But two configurations of sp^2-C and sp^3-C in the carbon skeleton often take the weak activity in multi-electrons catalysis. ACs with nitrogen doping could facilitate ionic diffusion and mass transfer[6-8], thus high energy and power density of supercapacitor can be supported[17,18].

Large surface area of AC relates to the abundant micropores, which may fully infiltrate electrolyte to improve the capacitance[19-21]. Their efficient microporous channels also help the air participate in oxygen reduction reaction (ORR)[22]. Meanwhile, the heteroatoms from the biomass could readjust the charge distribution in AC matrix, then promote electroactivity[23,24]. Therefore, an appropriate activation process for both enhancing surface area of AC and balancing the heteroatoms doping is expected.

In general, the technique for creating AC with desirable feature relates to the physical activation and the chemical activation. Through KOH activation, the high surface area of AC with defects could be created[25-27], but reducing the amount of KOH is necessary to alleviate the corrosion of equipment[19,28,29]. Not like the chemical activation, CO_2 activation is a green way to construct AC with micropores through adjusting the flow rate of CO_2 gas, temperature and reaction time[30-32]. But the yield of AC could decrease during the CO_2 consumption, and underdeveloped porous structure causes low specific surface area (SSA) of AC[31,33-34]. Some reports had constructed AC by combining CO_2 activation with KOH activation[35,36], but the carbon source and activation protocol leave a big unknown to the features of products.

Herein, we prepared nitrogen doped AC from cotton stalk through the KOH or CO_2 activation. The AC derived from KOH activation brought large SSA and pore volume. CO_2 activation led to a low SSA but a high nitrogen content of AC. The X-ray photoelectron spectroscopy (XPS) investigation suggested the species of nitrogen atoms. Combined with the physical features of AC, the electrochemical activities were improved in supercapacitor and oxygen evolution reaction (OER) procedure.

2. Experimental details

All the chemicals used were purchased from Sigma Aldrich Co. Ltd without any pretreatment.

2.1 Synthesis of AC Catalysts

The cotton stalk was provided from Xinjiang (Hongruida Fiber Co. Ltd.) and cleaned with water to remove the surface dust. Then the cleaned material was soaked in 2 mol • L^{-1} of acetic acid solution for 24 h, and washed with deionized water till to a neutral pH. After drying at 80 °C overnight, the carbonization procedure was carried out, the temperature was raised to 500 °C for 2 h in a tube furnace at a heating rate of 10 °C • min^{-1} and nitrogen flow of 60 mL • min^{-1}. Then the carbonized AC was used for activation.

2.1.1 CO_2 activation

2 g of carbonized AC was heated to 800 °C with a heating rate (10 °C • min^{-1}) under N_2 gas flow (60 mL • min^{-1}). CO_2 gas was flowed into the tube furnace for 2 h and with a flow rate of 150 mL • min^{-1}. After cooling down the sample was washed with 1 mol • L^{-1} of HCl and deionized water until to a neutral pH, finally the sample was collected after drying and named pAC.

2.1.2 KOH activation

The carbonized AC was mixed with two mass ratio of KOH, 20 mL of distilled water was added and stirred overnight for 12 h at room temperature, then the mixture was activated in a tube furnace at 800 °C for 2 h with a heating rate of 10 °C • min^{-1} and nitrogen flow of 60 mL • min^{-1}. Then the sample was washed as mentioned above. Finally the collected carbon was named cAC.

2.2 Characterizations

Nitrogen adsorption-desorption isotherms were measured by a Quantachrome Autosorb-1 MP sorption Analyzer at liquid-N_2 temperature (-196 ºC). The surface areas were calculated by Brunauer-Emmett-Teller (BET) method. The pore size distribution was deduced by Non-Local Density

Functional Theory (NLDFT)[37]. The JSM-6490LV scanning electron microscope (SEM) was used to observe the surface morphology. The transmission electron microscope (TEM JEM 1010) recorded the microstructure of samples. Raman scattering spectra were recorded by Renishaw InVia with 532 nm excitation light source in the range of 3500-400 cm^{-1}. Three times of scanning was set and the spectral resolution was 0.1 cm^{-1}. The XPS analysis to the carbon surface chemistry was performed by the physical electronics spectrometer (Thermo ESCALAB 250). The sample chamber was evacuated to 5.2×10^{-9} mbar and irradiated by a monochromatic Al *Kα* radiation (150 W, 15 kV, and 1486.6 eV). High resolution spectra were recorded at a fixed angle of 90º with respect to the sample surface. The spectrometer energy scale was calibrated using C1s (284.6 eV).

2.3 Working Electrode Tests

2.3.1 Supercapacitor

Nickel foam was selected as the working electrode collector with 1 cm^2 of active area. Ethanol was used as the dispersible solvent. AC was mixed with acetylene black and polytetrafluoroethylene (60 wt%) with the mass ratio of 75:20:5, and pressed under 20 MPa pressure for 30 s to form an electrode. The mass loading of AC was about 5 mg. Before test the work electrode was fully infiltrated in 6 mol • L^{-1} of KOH electrolyte for 10 h. The galvanostatic discharge-charge cycling tests were measured on LAND testing system.

Cyclic voltammetry (CV) and electrochemical impedance spectroscopy (EIS) were investigated by an IM6&ZENNIUM electrochemical workstation, measured in a three electrode system and the electrolyte was 6 mol • L^{-1} of KOH. Hg/HgO (1 mol • L^{-1} of KOH as internal solution) was chosen as a reference electrode and the counter electrode was a platinum electrode[38]. EIS was recorded at open circuit voltage, the frequency was set from 10 mHz to 100 kHz under disturbance voltage of 5 mV.

In a three electrode system, the capacitance value of ACs was calculated following the equation (1). The specific capacitance of the two electrode ACs was obtained with the equation (2). The energy density (E) and power density (P) were derived from the equation (3) and (4):

$$C = \frac{I\Delta t}{m\Delta \mathrm{v}} \quad (1)$$

$$C = \frac{2I\Delta t}{m\Delta \mathrm{v}} \quad (2)$$

$$E = \frac{1}{2*3.6} C\Delta \mathrm{V}^2 \quad (3)$$

$$P = \frac{3600E}{\Delta t} \quad (4)$$

Where the C is the specific capacitance (F • g^{-1}), I is the electric current (A), Δt is the discharge time (s), m is the mass of active carbon (g), ΔV is potential difference (V), E is energy density (Wh • kg^{-1}), P is power density (W • kg^{-1}), Δt is discharge time (s). The mass (m) in equation (2) is average mass of symmetric electrodes (g), and the C in equation (3) is calculated from the two-electrode system.

2.3.2 OER

The electrochemical tests of the samples were recorded at room temperature under a three electrode alkaline system. All electrochemical data was collected under steady-state conditions by cyclic scanning. 1 mol • L^{-1} of KOH (pH = 14) was set as the electrolyte, An electrode Hg/HgO (1 mol • L^{-1} of KOH as internal solution) and a platinum electrode were used as the reference and counter electrode, respectively[39]. The working electrode was prepared by the mixture of AC, Acetylene black and Polyvinylidene fluoride (PVDF HSV900) binder with a mass ratio of 8:1:1, which was then dispersed in N-methyl-2-pyrrolidinone (NMP) through grinding and pasted onto the nickel foam (current collector) with the total surface area of 2×1 cm^2, the loading mass of AC was about 10 mg. Linear sweep voltammetry (LSV) was tested at 5 mV • s^{-1} of sweep rate. The electric double layer capacitance was determined through the CV at the voltage window ranging from 0.925 V to 0.975 V *vs*. Reversible Hydrogen Electrode (RHE). The potential conversion was following the equation: $E_{(RHE)}=E_{(Hg/HgO)} + 0.059\ pH + 0.098$. The stability of the catalysts in OER was tested by chronoamperometry at the current density of 10 mA • cm^{-2}. Electrochemical impedance was collected at a potential of 1.63 V *vs*. RHE with the frequency range from 10 mHz to 100 kHz under the disturbance voltage of 5 mV.

3. Results and Discussion

3.1 Physical Properties of the Material

The surface area, pore volume and pore distribution of pAC and cAC have been summarized by N_2 adsorption-desorption measurement. In **Figure 1a** type I isotherms appear for pAC and cAC with a steep slope

at low relative pressures ($p/p_0 < 0.1$)[39]. cAC exhibits a S_{BET} of 1555 $m^2 \cdot g^{-1}$ with the V_{total} of 0.921 $cm^3 \cdot g^{-1}$. While, pAC has a S_{BET} of 538 $m^2 \cdot g^{-1}$ with the V_{total} of 0.360 $cm^3 \cdot g^{-1}$. The pore size distribution calculated by NLDFT method is at around 1 nm in **Figure 1b**. The results indicate that the KOH activation with etching reaction could provide a high surface area and large pore volume[26,40,41].

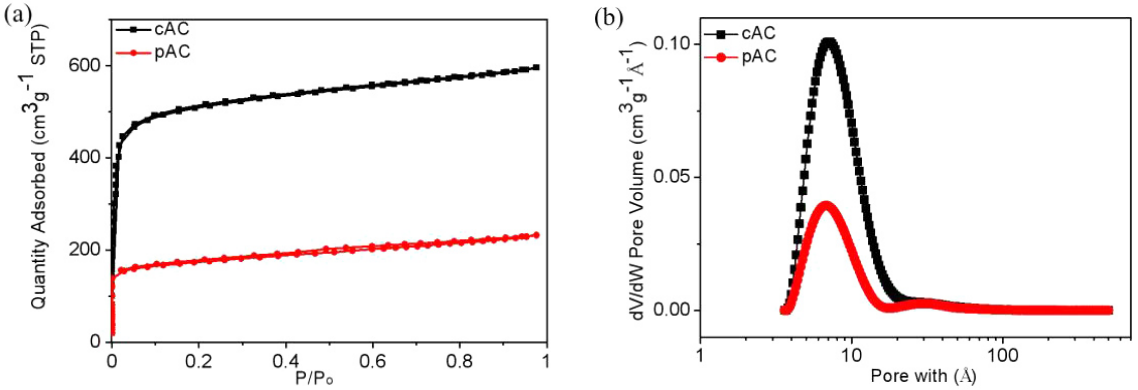

Figure 1. (a) Nitrogen adsorption-desorption isotherms; (b) Pore size distributions of cAC and pAC

The Raman spectra could be used to identify the disorder of carbon structure according to the intensity ratio of D band to G band (I_D/I_G) of which the D band around 1350 cm^{-1} relates to sp^3 carbon structure and the G band at 1580 cm^{-1} corresponds to the sp^2 bonded carbon[42]. The I_D/I_G values of cAC and pAC are 1.07 and 0.98, respectively as shown in **Figure S1**, confirming that more defects in the carbon framework of cAC than that of pAC.

The morphology of pAC and cAC was observed by the SEM and TEM as represented in **Figure 2a-2d**. The cAC displays less compact morphology than pAC. We can clearly observe the macropores at about 500 nm in cAC (**Figure 2a**). The macropores of pAC are about 1 μm and 240 nm (**Figure 2b**). TEM images of cAC and pAC represent the micropores at around 1 nm with uniform pore structure in **Figure 2c and 2d**. The wormhole like pores exist in the sample, which is beneficial to electrolyte infiltration and charge transfer process[43].

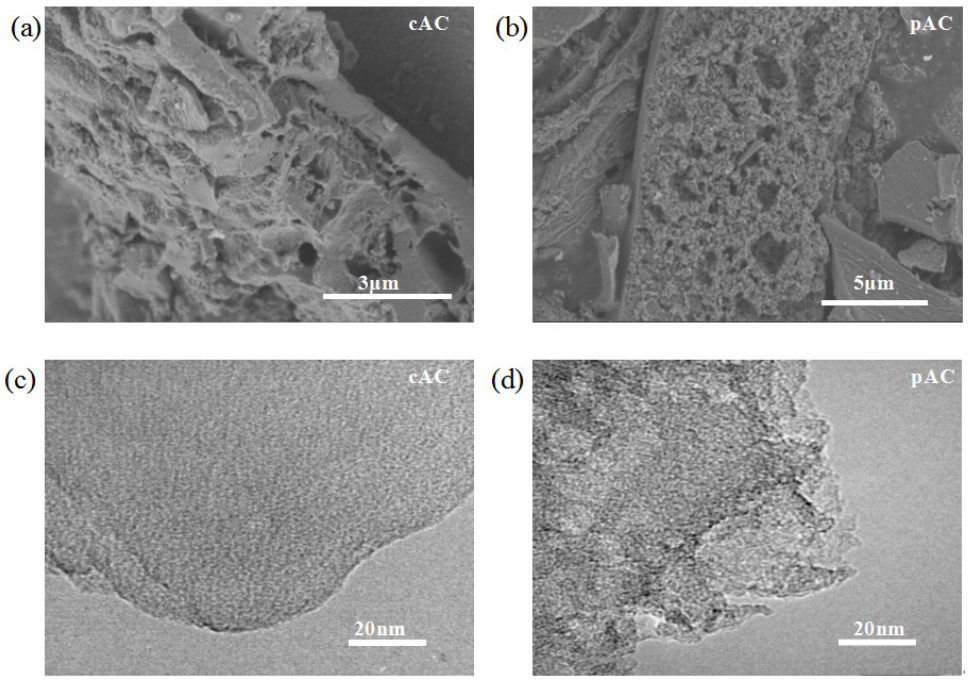

Figure 2. (a-b) SEM images; (c-d) TEM image of cAC and pAC

The surface chemistry of cAC and pAC was investigated by XPS. As shown in **Figure S2**, the content of C1s, N1s and O1s in cAC varies from that of pAC. The C1s spectra of the samples in **Figure S3** could be deconvoluted into four bonding configurations, C=C, CO/C–N, C=O/C=N and O–C=O, at the binding energy around 284.6, 285.5, 286.8 and 289.1 eV, respectively[3,44]. The O1s spectra of cAC and pAC are divided into four peaks at 531.5, 532.5, 533.7, 534.7, corresponding to the group of O=C, O–C, O–N, and water or chemisorbed O_2/CO_2[26] as shown in **Figure 3a and 3b**. The surface content of N is 2.15 at% and 3.53 at% for cAC and pAC, respectively. N1s represents four groups of pyridine-N, pyrrole-N, graphitic-N and oxidized N at the peak of 398.7, 399.8, 401.5 and 402.9 eV, in **Figure 3c and 3d**, respectively[45]. High content of pyrrole-N (1.55 at%) is keped during KOH activation, inversely graphitic-N (2.03 at%) is main in pAC by CO_2 activation. All peaks information has been summarized in **Table S1**. Cao *et al*.[33] reported that AC by CO_2 activation possessed 2.5 at% of N and 5.8 at% of S, which was higher than the AC (2.17 at% N and 0.85 at% S) by KOH activation. It is clear that the physical activation avoid over consuming carbon atoms, benefiting the heteroatoms remain.

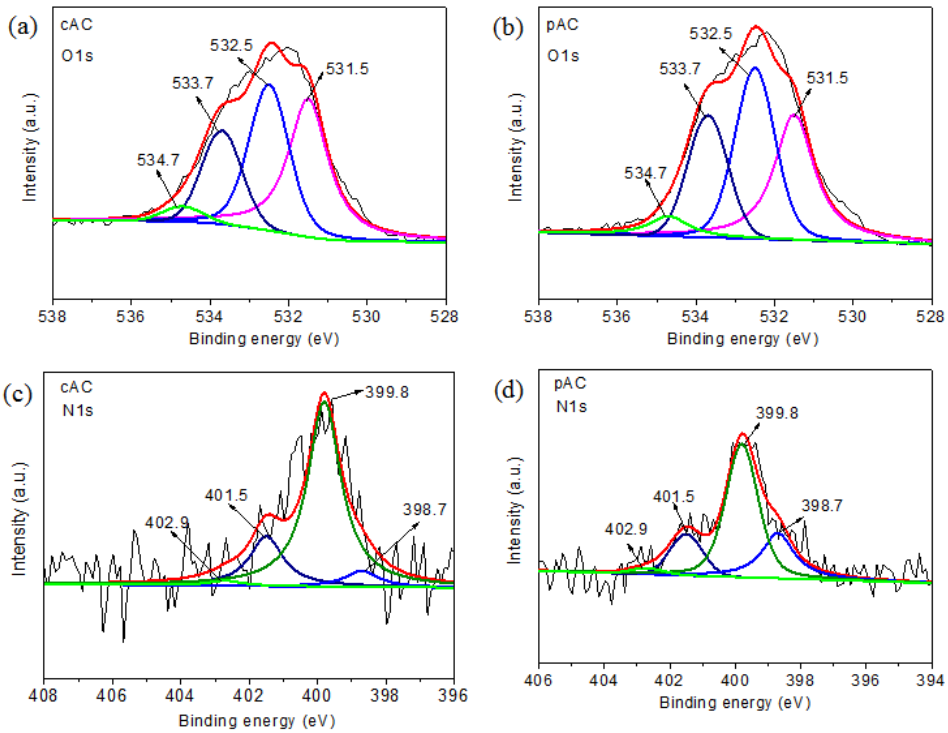

Figure 3. XPS high-resolution scans of cAC and pAC. O1s (a-b), N1s (c-d). The spectra were obtained by calibration based on C1s peak at 284.6 eV

3.2 Chemical Properties of the Material

3.2.1 Supercapacitor

Three electrode system in 6 mol • L^{-1} of KOH solution was adopted to evaluate supercapacitance of cAC and pAC. **Figure S4a and S4b** display the CV curves at the voltage range from -1 V to 0 V *vs*. Hg/HgO, using a scan rate range from 5 to 100 mV • s^{-1}. The CV curve is in approximate rectangle shape without linear polarization, indicating the feature of double-layer capacitor[46]. Galvanostatic charge-discharge (GCD) curves of cAC and pAC in **Figure S4c and S4d** were collected at different current densities. The cAC exhibits the capacitance of 286, 232, 200, 192 and 185 F • g^{-1} at 0.5, 1, 2, 3 and 5 A • g^{-1}, respectively. The specific capacitance pAC is 163 F • g^{-1} at current density of 0.5 A • g^{-1}, indicating that rich pore of the sample is good for electron transfer[47].

In a two-electrode system the GCD tests was recorded in 6 mol • L^{-1} of KOH. The calculated capacitance of pAC and cAC is 122 F • g^{-1} (**Figure**

4a) and 178 F • g^{-1} at the current density of 1 A • g^{-1} (**Figure 4b**). The ragone plot of **Figure 4c** reveals that the cAC has a high energy of 24 Wh • kg^{-1} and power density of 970 W • kg^{-1}, which is better than the AC made from pomelo peel (9.4 Wh • kg^{-1})[48] and the AC from soybean (12.5 Wh • kg^{-1} at a power density of 450 W • kg^{-1})[49]. Cyclic stability of cAC and pAC was tested by GCD test at a current density of 1 A • g^{-1}. **Figure S4e** shows that cAC electrode has the capacitance retention 74% after 1000 cycles GCD test, and the nearly capacitance retention 73% in cAC.

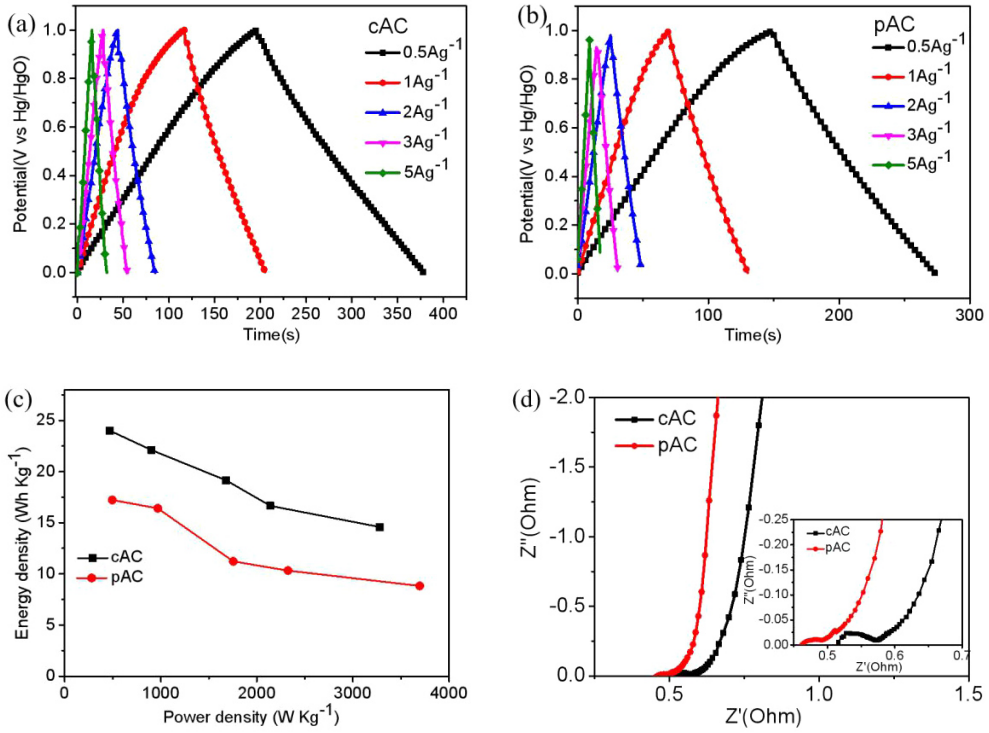

Figure 4. (a) and (b) Galvanostatic charge-discharge (GCD) curves of cAC and pAC in two- electrode system in 6 M KOH electrolyte; (c) The related ragone plot; (d) The EIS was recorded at open circuit voltage in 6 M KOH electrolyte by three electrode system; (inset) the enlarged EIS spectra at high frequency

The EIS was recorded at the open circuit voltage in **Figure 4d**. The curves of cAC and pAC display a semi arc in the high frequency region and a Warburg line in the low frequency region, corresponding to the dynamic processes of the charge transfer and the ions diffusion from electrolyte into the electrode[50]. The small semicircle diameter indicates a low electrical resistance and good electrical conductivity. The Warburg line is close to 90°, indicating the ideal capacitor behavior and the fast ion diffusion rate[51,52].

Benefited to the micropores, AC from wood fibers represented a high specific capacitance of 345 F • g^{-1} at 0.5 A • g^{-1}, of which the surface area was 1807 m^2 • g^{-1}[21]. AC from waste bones had a 1260 m^2 • g^{-1} of SSA, and a capacitance of 234 F • g^{-1} was obtained at 1 A • g^{-1} in 6 M KOH[25]. AC derived from natural casings displayed a specific capacitance of 190 F • g^{-1} at 1 A • g^{-1} and possessed a surface area of 2383 m^2 • g^{-1}[27]. Thus KOH activation is helpful to get a high capacitance. AC obtained in two mass ratio of KOH displayed a capacitance of 156 F • g^{-1} in 1 mol • L^{-1} of TEABF4/AN electrolyte. The surface area was 3386 m^2 • g^{-1} accompany with 0.58 at% of nitrogen. As a comparison, 0.5 mass ratio of KOH promoted AC a surface area of 768 m^2 • g^{-1} and 5.12 at% nitrogen. Its capacitance was only 60 F • g^{-1}[19]. By CO_2 activation, 1.81 at% nitrogen doped AC from date fruit with SSA 464 m^2 • g^{-1} showed a capacitance of 103 F • g^{-1} at 1 mV • s^{-1} in 6 mol • L^{-1} of KOH[34]. 2.25 at% nitrogen doped carbon aerogel with the SSA of 1415 m^2 • g^{-1} from banana flesh achieved a capacitance of 179 F • g^{-1} at 1A • g^{-1}[31]. What's more, the usage of KOH does not need a high ratio. The cAC has a prominent capacitance than the AC from Konjaku flour (216 F • g^{-1}), even through five mass ratio KOH was used[47]. By testing

the electrochemical feature of rice husk-based hierarchical porous carbon, Chen *et al*.[53] proposed that a suitable pore size distribution is essential for the high capacitance and excellent rate capability.

3.2.2 The OER test

The OER activity of the cAC was evaluated by LSV curves at a scan rate of 5 mV • s^{-1}. **Figure 5a** suggests that cAC exhibits the lowest onset potential, which is even lower than the IrO_2. Especially, at the current density of 10 mA • cm^{-2}, the overpotential of cAC, pAC and IrO_2 is 230, 366 and 290 mV, respectively. The Tafel slop reflects a specific rate of determining steps for the four electron transfer process in the OER, according to the convert formula $\eta=a+b\log J$ (where a and b are the constant number in the linear curve) [25]. As shown in **Figure 5b**, the cAC and pAC displays the slope of 297 mV • s^{-1} and 339 mV • s^{-1}, reflecting that the adsorption of OH^- ion is the rate-determining step in OER[54,55]. The OER stability is reflected by the chronoamperometry method at the current density of 10mA • cm^{-2}. The plot in **Figure 5c** represents the voltage changing in the constant current discharge, the voltage rises first and then the potential has the fluctuation of 100 mV within 30,000 s, the clear transparent electrolyte gradually turns into light brown. The similar results has been observed in activated carbon cloth[56]. The electrochemical double-layer capacitance (C_{dl}) derived from the CV tests is under different scans (2, 4, 6, 8, and 10 mV • s^{-1}) at the voltage of 0.955 V (*vs*. RHE) in **Figure S5**. The C_{dl} value of cAC and pAC is 275 mF • cm^{-2} and 119 mF • cm^{-2}, respectivley, which confirms that the cAC is more active than pAC (**Figure 5** inset)[57]. For OER process those active sites lowers the overpotential, leading to the cAC better than the pAC.

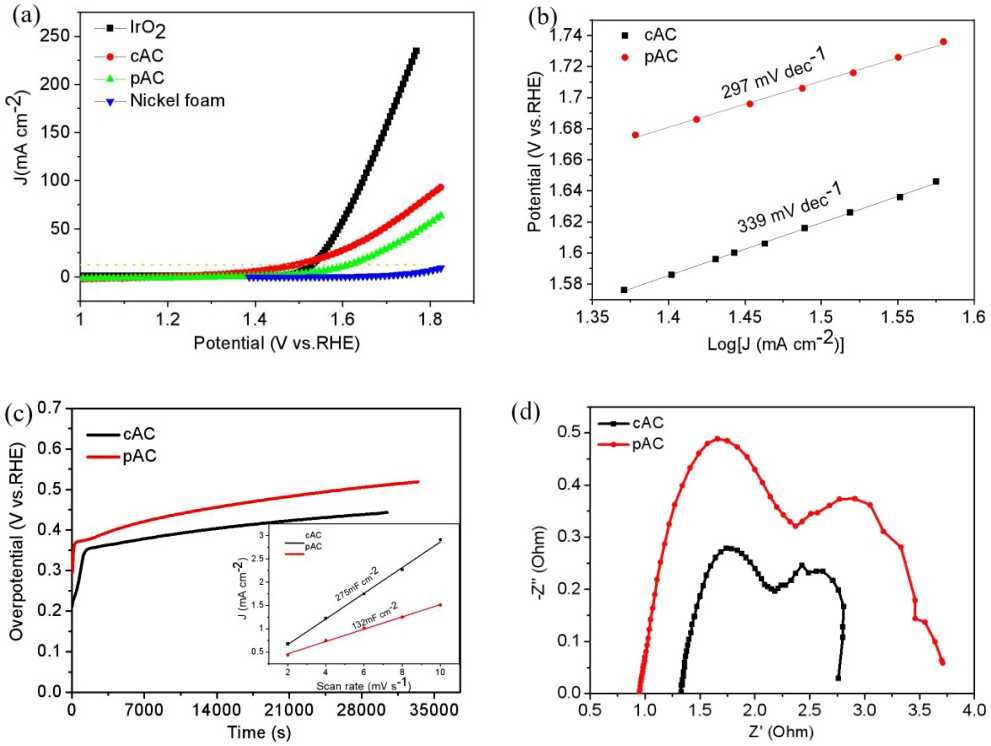

Figure 5. OER performance (a) polarization curves of cAC and pAC at a scan rate of 5 mV/s; (b) Tafel plots; (c) the chronoamperometry was recorded at the current density of 10 mA/cm^2, and the value of calculated C_{dl} are inserted; (d) EIS of the ACs recorded at 1.63 V *vs*. RHE

To observe the surface charge motion of the electrode during OER process, EIS of the ACs samples were measured at 1.63 V *vs*. RHE in 1 mol • L^{-1} of KOH. As shown in **Figure 5d**, cAC and pAC present the two semicircles from 10 mHz to 100 kHz, corresponding to the charge transfer process at high frequency region and the Gerischer impedance[58] at low frequency region, respectively. The small semicircle relates to the high conductivity. It is clear that cAC is more active than the pAC[59].

The low overpotential of cAC could be ascribed to its high surface area and functional groups. ZnO@ carbon microbeads displayed improved ethanol electrooxidation with a low onset potential 0.4 V (*vs*. Ag/AgCl)[60]. The spent coffee ground was used as the carbon source and $ZnCl_2$ was the active agent. On the contrary the non-activated carbon from spent coffee ground had no any activity to the ethanol electrooxidation. It is clear that the activation is important to enhance the surface area and enrich the surface functional group. Although the physical activation could keep more functional groups on the carbon surface, the limited surface area and pore volume are the fatal weakness to achieve the requirement of electro-oxidation. The cAC obtained with KOH activation possesses the advantage of high surface, large pore volume, and rich pyrolle-N, those are responsible to promote the OER.

4. Conclusion

The cotton stalk is used to prepare the AC with physical and chemical activation method, leading to a special feature on the carbon framework. High nitrogen content exists in the CO_2 activated carbon pAC with 3.53 at%. Although KOH activated carbon cAC displays a low nitrogen content (2.15 at%), it possesses a high surface area with 1555 $m^2 \cdot g^{-1}$, that promots an interesting activity in supercapacitor and OER reaction. The cAC packed supercapacitor possesses a high capacitance and the OER performance of cAC shows a low overpotential of 230 mV *vs*. RHE at 10 mA $\cdot$ cm^{-2} owning to the existence of rich micropores and surface functional groups. XPS analysis reveals that the pyrrole-N is formed during the KOH activation. Combining with high specific surface area AC, the carbon by KOH activation would be actively responsible to the application of renewable energy conversion and storage.

Acknowledgement

This work was supported by the Foundation of State Key Laboratory of High-efficiency Utilization of Coal and Green Chemical Engineering (2020-KF-22), the Natural Science Foundation of Xinjiang Uygur Autonomous Region (2021D01A03) and Key Research and Development Projects of Xinjiang Uygur Autonomous Region(2022B02038).

References

[1] Yang L, Shui J, Du L, *et al*. Carbon-based metal-free ORR electrocatalysts for fuel cells: past, present, and future. *Advanced Materials*, 2019;31(13):1804799. https://doi.org/10.1002/adma.201804799

[2] Li Q, He T, Zhang YQ, *et al*. Biomass waste-derived 3D metal-free porous carbon as a bifunctional electrocatalyst for rechargeable zinc-air batteries. *ACS Sustainable Chemistry & Engineering*, 2019;7(20):17039-17046. https://doi.org/10.1021/acssuschemeng.9b02964

[3] Liu Z, Li Z, Tian S, *et al*. Conversion of peanut biomass into electrocatalysts with vitamin B12 for oxygen reduction reaction in Zn-air battery. *International Journal of Hydrogen Energy*, 2019;44(23):11788-11796. https://doi.org/10.1016/j.ijhydene.2019.03.055

[4] Ren JT, Yuan GG, Weng CC, *et al*. Hierarchically porous heteroatoms-doped vesica-like carbons as highly efficient bifunctional electrocatalysts for Zn-air batteries. *ChemCatChem*, 2018;10(22):5297-5305. https://doi.org/10.1002/cctc.201801482

[5] Zhu X, Li Y, Li R, *et al*. Self-assembled N-doped carbon with a tube-in-tube nanostructure for lithium-sulfur batteries. *Journal of Colloid and Interface Science*, 2020;559:244-253. https://doi.org/10.1016/j.jcis.2019.10.027

[6] Kang MS, Heo I, Cho KG, *et al*. Coarsening-induced hierarchically interconnected porous carbon polyhedrons for stretchable ionogel-based supercapacitors. *Energy Storage Materials*, 2022;45:380-388. https://doi.org/10.1016/j.ensm.2021.12.001

[7] Sajjadi B, Chen WY and Egiebor NO. A comprehensive review on physical activation of biochar for energy and environmental applications. *Reviews in Chemical Engineering*, 2019;35(6):735-776. https://doi.org/10.1515/revce-2017-0113

[8] Wang S, Liu Y, Wang Q, *et al*. Fabrication of self-doped aramid-based porous carbon fibers for the high-performance supercapacitors. *Journal of Electroanalytical Chemistry*, 2022;923:116829. https://doi.org/10.1016/j.jelechem.2022.116829

[9] Wang X, Vasileff A, Jiao Y, *et al*. Electronic and structural engineering of carbon-based metal-free electrocatalysts for water splitting. *Advanced Materials*, 2019;31(13):1803625. https://doi.org/10.1002/adma.201803625

[10] Jayaraman T, Murthy AP, Elakkiya V, *et al*. Recent development on carbon based heterostructures for their applications in energy and environment: a review. *Journal of Industrial and Engineering Chemistry*, 2018;64:16-59. https://doi.org/10.1016/j.jiec.2018.02.029

[11] Creutzig F, Breyer C, Hilaire J, *et al*. The mutual dependence of negative emission technologies and energy systems. *Energy & Environmental Science*, 2019;12(6):1805-1817. https://doi.org/10.1039/C8EE03682A

[12] Gao Z, Zhang Y, Song N, *et al*. Biomass-derived renewable carbon materials for electrochemical energy storage. *Materials Research Letters*, 2017;5(2):69-88. https://doi.org/10.1080/21663831.2016.1250834

[13] Chinnadurai D, Karuppiah P, Chen SM, *et al*. Metal-free multiporous carbon for electrochemical energy storage and electrocatalysis applications. *New Journal of Chemistry*, 2019;43(29):11653-11659. https://doi.org/10.1039/C9NJ01875A

[14] Zhou S, Zhou L, Zhang Y, *et al*. Upgrading earth-abundant biomass into three-dimensional carbon materials for energy and environmental applications. *Journal of Materials Chemistry A*, 2019;7(9):4217-4229. https://doi.org/10.1039/C8TA12159A

[15] Hu C and Dai L. Multifunctional carbon-based metal-free electrocatalysts for simultaneous oxygen reduction, oxygen evolution, and hydrogen evolution. *Advanced Materials*, 2017;29(9):1604942. https://doi.org/10.1002/adma.201604942

[16] Bi Z, Kong Q, Cao Y, *et al*. Biomass-derived porous carbon materials with different dimensions for supercapacitor electrodes: a review. *Journal of Materials Chemistry A*, 2019;7(27):16028-16045. https://doi.org/10.1039/C9TA04436A

[17] Xu Z, Chen J, Zhang X, *et al*. Template-free preparation of nitrogen-doped activated carbon with porous architecture for high-performance supercapacitors. *Microporous and Mesoporous Materials*, 2019;276:280-291. https://doi.org/10.1016/j.micromeso.2018.09.023

[18] Liu Y, Qiu X, Liu X, *et al*. 3D porous binary-heteroatom doped carbon nanosheet/electrochemically exfoliated graphene hybrids for high performance flexible solid-state supercapacitors. *Journal of Materials Chemistry A*, 2018;6(18):8750-8756. https://doi.org/10.1039/C8TA01148F

[19] Sun J, Niu J, Liu M, *et al*. Biomass-derived nitrogen-doped porous carbons with tailored hierarchical porosity and high specific surface area for high energy and power density supercapacitors. *Applied Surface Science*, 2018;427:807-813. https://doi.org/10.1016/j.apsusc.2017.07.220

[20] Zou J, Tu W, Zeng SZ, *et al*. High-performance supercapacitors based on hierarchically porous carbons with a three-dimensional conductive network structure. *Dalton Transactions*, 2019;48(16):5271-5284. https://doi.org/10.1039/C9DT00261H

[21] Liu F, Gao Y, Zhang C, *et al*. Highly microporous carbon with nitrogen-doping derived from natural biowaste for high-performance flexible solid-state supercapacitor. *Journal of Colloid and Interface Science*, 2019;548:322-332. https://doi.org/10.1016/j.jcis.2019.04.005

[22] Eom SW, Lee CW, Yun MS, *et al*. The roles and electrochemical characterizations of activated carbon in zinc air battery cathodes. *Electrochimica Acta*, 2006;52(4):1592-1595. https://doi.org/10.1016/j.electacta.2006.02.067

[23] Zhang LY, Wang MR, Lai YQ, *et al*. Nitrogen-doped microporous carbon: an efficient oxygen reduction catalyst for Zn-air batteries. *Journal of Power Sources*, 2017;359:71-79. https://doi.org/10.1016/j.jpowsour.2017.05.056

[24] He J, Zhang D, Han M, *et al*. One-step large-scale fabrication of nitrogen doped microporous carbon by self-activation of biomass for supercapacitors application. *Journal of Energy Storage*, 2019;21:94-104. https://doi.org/10.1016/j.est.2018.11.015

[25] Niu L, Shen C, Yan L, *et al*. Waste bones derived nitrogen-doped carbon with high micropore ratio towards supercapacitor applications. *Journal of Colloid and Interface Science*, 2019;547:92-101. https://doi.org/10.1016/j.jcis.2019.03.097

[26] Xu SS, Qiu SW, Yuan ZY, *et al*. Nitrogen-containing activated carbon of improved electrochemical performance derived from cotton stalks using indirect chemical activation. *Journal of Colloid and Interface Science*, 2019;540:285-294. https://doi.org/10.1016/j.jcis.2019.01.031

[27] Xu Z, Li Y, Li D, *et al*. N-enriched multilayered porous carbon derived from natural casings for high-performance supercapacitors. *Applied Surface Science*, 2018;444:661-671. https://doi.org/10.1016/j.apsusc.2018.03.100

[28] Huang J, Wu J, Dai F, *et al*. 3D honeycomb-like carbon foam synthesized with biomass buckwheat flour for high-performance supercapacitor electrodes. *Chemical Communications*, 2019;55(62):9168-9171. https://doi.org/10.1039/C9CC03039E

[29] Li YT, Pi YT, Lu LM, *et al*. Hierarchical porous active carbon from fallen leaves by synergy of K_2CO_3 and their supercapacitor performance. *Journal of Power Sources*, 2015;299:519-528. https://doi.org/10.1016/j.jpowsour.2015.09.039

[30] Pallarés J, González-Cencerrado A and Arauzo I. Production and characterization of activated carbon from barley straw by physical activation with carbon dioxide and steam. *Biomass and Bioenergy*, 2018;115:64-73. https://doi.org/10.1016/j.biombioe.2018.04.015

[31] Lei E, Li W, Ma C, *et al*. CO_2-activated porous self-templated N-doped carbon aerogel derived from banana for high-performance supercapacitors. *Applied Surface Science*, 2018;457:477-486. https://doi.org/10.1016/j.apsusc.2018.07.001

[32] Yu M, Han Y, Li J, *et al*. CO_2-activated porous carbon derived from cattail biomass for removal of malachite green dye and application as supercapacitors. *Chemical Engineering Journal*, 2017;317:493-502. https://doi.org/10.1016/j.cej.2017.02.105

[33] Cao Y, Ning G, Xu C, *et al*. Selective activation of S or N-containing carbon segments by alkalic or acidic activators. *Industrial & Engineering Chemistry Research*, 2019;58(21):9048-9055. https://doi.org/10.1021/acs.iecr.9b00306

[34] Kirubakaran CJ, Krishnaiah K and Seshadri SK. Experimental study of the production of activated carbon from coconut shells in a fluidized bed reactor. *Industrial & Engineering Chemistry Research*, 1991;30(11):2411-2416. https://doi.org/10.1021/ie00059a008

[35] Taer E, Manik ST, Taslim R, *et al*. Preparation of activated carbon monolith electrodes from sugarcane bagasse by physical and physical-chemical activation process for supercapacitor application. *Advanced Materials Research*, 2014;896:179-182. https://doi.org/10.4028/www.scientific.net/AMR.896.179

[36] Farma R, Deraman M, Awitdrus A, *et al*. Preparation of highly porous binderless activated carbon electrodes from fibres of oil palm empty fruit bunches for application in supercapacitors. *Bioresource Technology*, 2013;132:254-261. https://doi.org/10.1016/j.biortech.2013.01.044

[37] Landers J, Gor GY and Neimark AV. Density functional theory methods for characterization of porous materials. *Colloids and Surfaces A: Physicochemical and Engineering Aspects*, 2013;437:3-32. https://doi.org/10.1016/j.colsurfa.2013.01.007

[38] Li K, Ren T, Yuan ZY, *et al*. Electrodeposited PCo nanoparticles in deep eutectic solvents and their performance in water splitting. *International Journal of Hydrogen Energy*, 2018;43(22):10448-10457. https://doi.org/10.1016/j.ijhydene.2018.04.136

[39] Rouquerol J, Avnir D, Fairbridge CW, *et al*. Recommendations for the characterization of porous solids (Technical Report). *Pure and Applied Chemistry*, 1994;66(8):1739-1758. https://doi.org/10.1351/pac199466081739

[40] Pi YT, Xing XY, Lu LM, *et al*. Hierarchical porous activated carbon in OER with high efficiency. *RSC Advances*, 2016;6(104):102422-102427. https://doi.org/10.1039/C6RA19333A

[41] Wang W, Xu S, Wang K, *et al*. De-intercalation of the intercalated potassium in the preparation of activated carbons by KOH activation. *Fuel Processing Technology*, 2019;189:74-79. https://doi.org/10.1016/j.fuproc.2019.03.001

[42] Cho NH, Veirs DK, Ager Iii JW, *et al*. Effects of substrate temperature on chemical structure of amorphous carbon films. *Journal of Applied Physics*, 1992;71(5):2243-2248. https://doi.org/10.1063/1.351122

[43] Jin K, Zhang W, Wang Y, *et al*. In-situ hybridization of polyaniline nanofibers on functionalized reduced graphene oxide films for high-performance supercapacitor. *Electrochimica Acta*, 2018;285:221-229. https://doi.org/10.1016/j.electacta.2018.07.220

[44] Li Y, Zhu G, Huang H, *et al*. A N, S dual doping strategy via electrospinning to prepare hierarchically porous carbon polyhedra embedded carbon nanofibers for flexible supercapacitors. *Journal of Materials Chemistry A*, 2019;7(15):9040-9050. https://doi.org/10.1039/C8TA12246F

[45] Chen Y, Li X, Park K, *et al*. Nitrogen-doped carbon for sodium-ion battery anode by self-etching and graphitization of bimetallic MOF-based composite. *Chem*, 2017;3(1):152-163. https://doi.org/10.1016/j.chempr.2017.05.021

[46] Chen H, Chen J, Chen D, *et al*. Nitrogen-and oxygen-rich dual-decorated carbon materials with porosity for high-performance supercapacitors. *Journal of Materials Science*, 2019;54(7):5625-5640. https://doi.org/10.1007/s10853-018-2993-x

[47] Lin XQ, Lü QF, Li Q, *et al*. Fabrication of low-cost and ecofriendly porous biocarbon using konjaku flour as the raw material for high-performance supercapacitor application. *ACS Omega*, 2018;3(10):13283-13289. https://doi.org/10.1021/acsomega.8b01718

[48] Liang Q, Ye L, Huang ZH, *et al*. A honeycomb-like porous carbon derived from pomelo peel for use in high-performance supercapacitors. *Nanoscale*, 2014;6(22):13831-13837. https://doi.org/10.1039/C4NR04541F

[49] Lin G, Ma R, Zhou Y, *et al*. KOH activation of biomass-derived nitrogen-doped carbons for supercapacitor and electrocatalytic oxygen reduction. *Electrochimica Acta*, 2018;261:49-57. https://doi.org/10.1016/j.electacta.2017.12.107

[50] Wang B, Ji L, Yu Y, *et al*. A simple and universal method for preparing N, S co-doped biomass derived carbon with superior performance in supercapacitors. *Electrochimica Acta*, 2019;309:34-43. https://doi.org/10.1016/j.electacta.2019.04.087

[51] Lei W, Guo J, Wu Z, *et al*. Highly nitrogen and sulfur dual-doped carbon microspheres for supercapacitors. *Science Bulletin*, 2017;62(14):1011-1017. https://doi.org/10.1016/j.scib.2017.06.001

[52] Chen Z, Wang X, Xue B, *et al*. Self-templating synthesis of 3D hollow tubular porous carbon derived from straw cellulose waste with excellent performance for supercapacitors. *ChemSusChem*, 2019;12(7):1390-1400. https://doi.org/10.1002/cssc.201802945

[53] Chen Z, Wang X, Xue B, *et al*. Rice husk-based hierarchical porous carbon for high performance supercapacitors: the structure-performance relationship. *Carbon*, 2020;161:432-444. https://doi.org/10.1016/j.carbon.2020.01.088

[54] Li G, Anderson L, Chen Y, *et al*. New insights into evaluating catalyst activity and stability for oxygen evolution reactions in alkaline media. *Sustainable Energy & Fuels*, 2018;2(1):237-251. https://doi.org/10.1039/C7SE00337D

[55] Doyle RL and Lyons MEG. The oxygen evolution reaction: mechanistic concepts and catalyst design. In: In: Giménez S, Bisquert J (editors). Photoelectrochemical solar fuel production. Springer, Cham; 2016. pp. 41-104.

[56] Huang D, Li S, Zhang X, *et al*. A novel method to significantly boost the electrocatalytic activity of carbon cloth for oxygen evolution reaction. *Carbon*, 2018;129:468-475. https://doi.org/10.1016/j.carbon.2017.12.046

[57] He D, Zhao W, Li P, *et al*. Bifunctional biomass-derived N, S dual-doped ladder-like porous carbon for supercapacitor and oxygen reduction reaction. *Journal of Alloys and Compounds*, 2019;773:11-20. https://doi.org/10.1016/j.jallcom.2018.09.141

[58] Wu H, Geng J, Ge H, *et al*. Egg-derived mesoporous carbon microspheres as bifunctional oxygen evolution and oxygen reduction electrocatalysts. *Advanced Energy Materials*, 2016;6(20):1600794. https://doi.org/10.1002/aenm.201600794

[59] Irshad A and Munichandraiah N. Electrochemical deposition of manganese oxide-phosphate-reduced graphene oxide composite and electrocatalysis of the oxygen evolution reaction. *RSC Advances*, 2016;6(36):30552-30563. https://doi.org/10.1039/C6RA01217E

[60] Ghouri ZK, Elsaid K, Abdel-Wahab A, *et al*. Electrooxidation behavior of ethanol toward carbon microbead-encapsulated ZnO

particles derived from coffee waste. *Journal of Materials Science: Materials in Electronics*, 2020;31(9):6530-6537. https://doi.org/10.1007/s10854-020-03209-w

Supporting Information

Table S1. The summary of quantitative elements and the fitting peak information of the cAC and pAC by XPS

Bond assignment	Binding energy (eV)	cAC (at%)	pAC (at%)
C1s		87.46	85.17
C=C sp^2	284.6	56.61	56.41
C–O (phenolic, alcoholic, ether), C–N (carbon-nitrogen structures)	285.5	11.46	15.07
O–C=O (carboxyl or ester)	286.8	9.74	8.57
π→π*, π-electrons in aromatic rings	289.1	9.65	5.12
O1s		10.39	11.30
O=C (in carboxyl/carbonyl)	531.5	4.35	3.93
O–C (in phenol/epoxy)	532.5	3.63	4.05
N–O	533.7	2.07	2.67
Water or chemisorbed O_2, CO_2	534.7	0.34	0.65
N1s		2.15	3.53
pyridine-N	398.7	0.42	0.54
pyrrole-N	399.8	1.55	0.87
graphitic-N	401.5	0.14	2.03
pyridine N^+–O^-	402.9	0.04	0.09

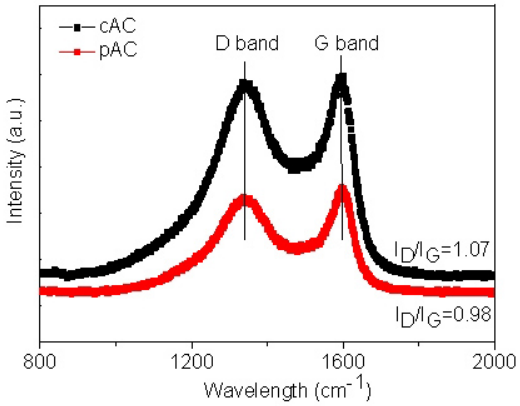

Figure S1. The Raman spectrum of the samples

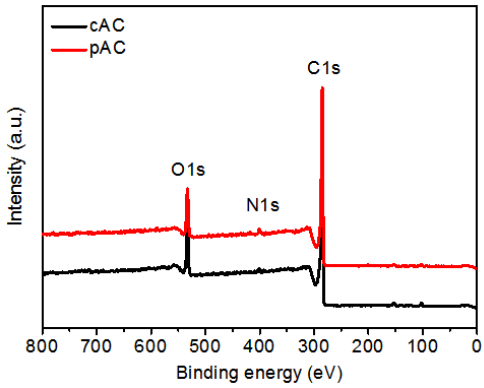

Figure S2. The survey spectrum of the samples exhibit the typical peaks C, N and O elements

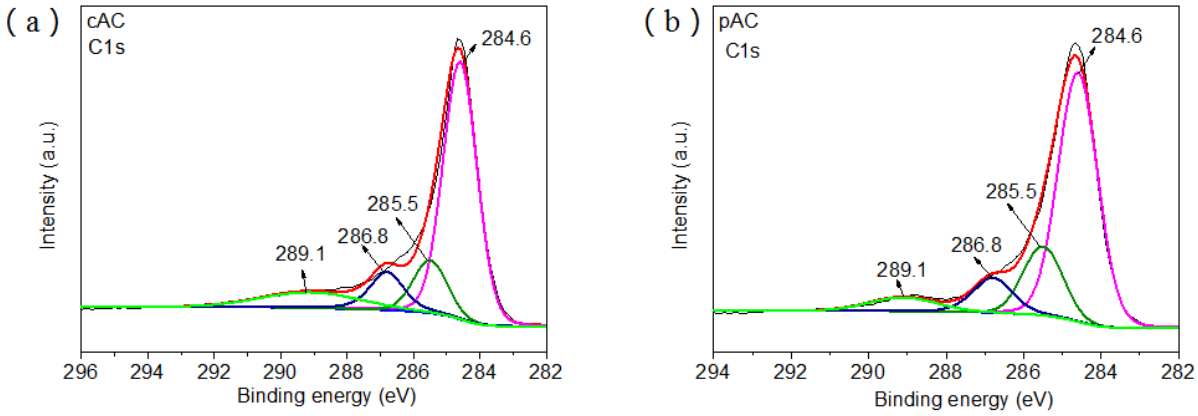

Figure S3. The C1s spectra of cAC (a) and pAC (b). The spectra were obtained by calibration based on C1s peak at 284.6 eV

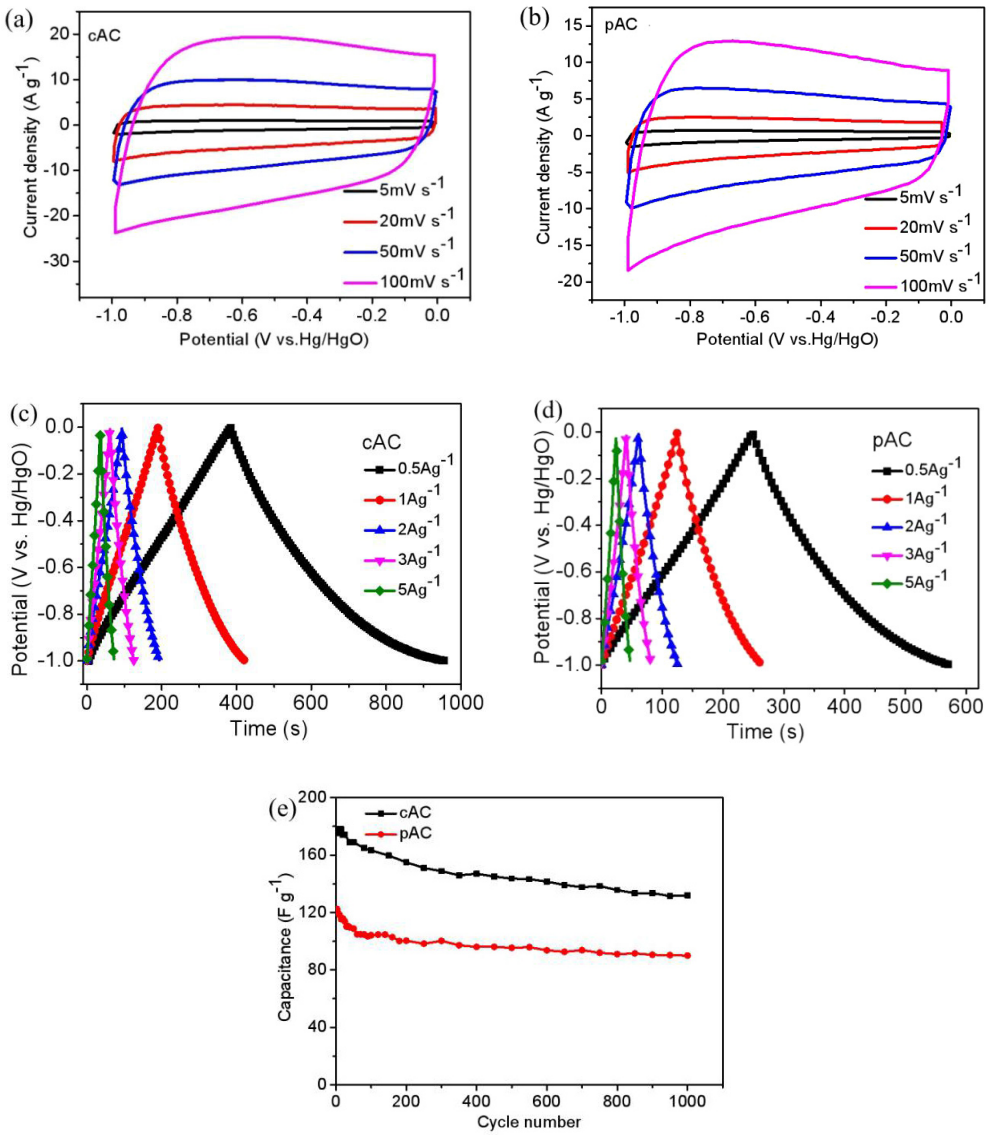

Figure S4. (a) and (b) displayed the cyclic voltammetry (CV) curves of cAC and pAC at three electrode system in 6 M KOH electrolyte, using a scan rate range from 5 mV/s to 100 mV/s; (c) and (d) galvanostatic charge-discharge (GCD) curves of cAC and pAC were collected at different current densities at three electrode system in 6 M KOH electrolyte; (e) cycle ability of the samples by GCD test at a current density of 1 A/g for 1000 cycles in two electrode cell

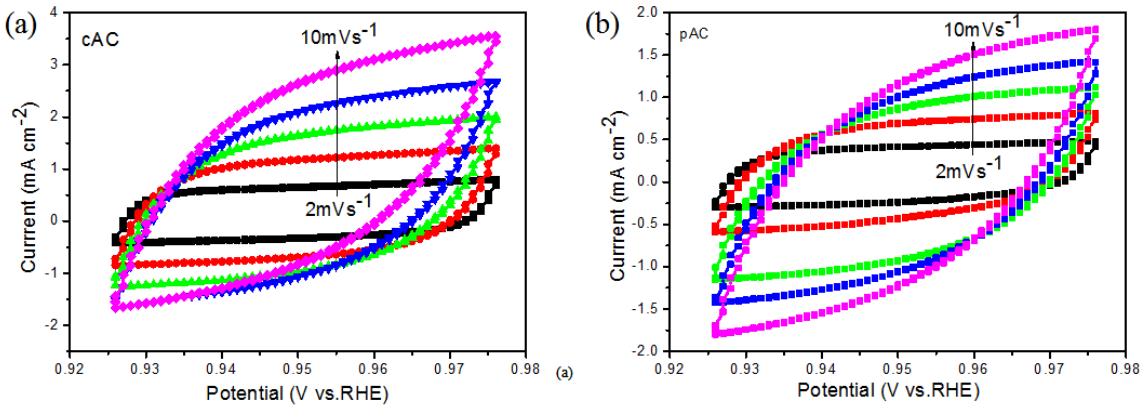

Figure S5. The CdI from CV tests were under different scans (2 mV/s, 4 mV/s, 6 mV/s, 8 mV/s, 10 mV/s) at the voltage of 0.955 V vs. RHE